



Formation Mechanisms of the Extreme Rainfall and Mesoscale Convective Systems over South China during the Dragon Boat Rainy Season of 2022

Yanan Fu^{1,2} · Jianhua Sun^{1,2} · Zhifang Wu³ · Tao Chen⁴ · Xiaodong Song⁵ · Shijun Sun⁵ · Shenming Fu¹

Received: 3 November 2023 / Revised: 28 February 2024 / Accepted: 4 March 2024

© The Author(s) under exclusive licence to Korean Meteorological Society and Springer Nature B.V. 2024

Abstract

The formation mechanisms of the record-breaking rainfall event during the Dragon Boat Rainy Season (DBRS) of 2022 are comprehensively analyzed from the synoptic scale and the mesoscale perspectives. The extreme rainfall event is characterized by the highest rainfall amount since 1981, and an abnormal spatial distribution with much higher (lower) rainfall amount in the northern (southern) part of South China. The abnormal circulation and thermodynamic conditions are mainly responsible for the extreme rainfall. The favorite synoptic condition for rainfall is the combination of warm advection, frontal forcing, orographic lifting and low-level jet favor the convection development. The similar configurations repeatedly impact South China during the DBRS of 2022, causing multiple heavy rainfall events, leading to the extreme rainfall of the whole period. The abnormal moisture convergence together with the frontal zone, which is stronger than the climatology, results in the rainfall centers over the northern part of South China. 54.35% of the rainfall amount is related to mesoscale convective systems (MCSs) which mainly originate from four regions. The MCSs from the four regions are characterized by different formation peaks, spatial scales, lifetimes and propagations. The large-scale warm and moist air mass, the moistening caused by synoptic advection and the local diabatic heating are responsible for the increasing instability for the MCSs. The low-level jets play an important role in the formation of MCSs by providing moisture. The thermodynamic (dynamic) environmental conditions control the formation of MCSs in the afternoon (night).

Keywords Dragon Boat Rainy Season · Pre-summer rainy season · Extreme rainfall · Mesoscale convective system

1 Introduction

The dragon boat rainy season (DBRS), typically from 21 May to 20 June, referring to the period of rainfall around the Dragon Boat Festival, is the predominant period of the

Communicated by Wei Wang.

✉ Jianhua Sun
sjh@mail.iap.ac.cn

- ¹ Institute of Atmospheric Physics, Chinese Academy of Sciences, Beijing, China
- ² University of Chinese Academy of Sciences, Beijing, China
- ³ Guangdong Meteorological Service, Guangzhou, Guangdong, China
- ⁴ National Meteorological Center, Beijing, China
- ⁵ State Grid Shandong Electric Power Company, Jinan, Shandong, China

pre-summer rainy season over South China (Cheng et al. 2023; Qian et al. 2021, 2020; Sheng et al. 2023; Wu et al. 2017; Lin et al. 2009; Hu et al. 2013). As the first stage of the summer monsoon rainfall in China, the rainfall during the DBRS is affected by the warm-moist air mass from the southwest, the baroclinic weather systems from the north and the complex topography of South China, resulting in long-lasting rainstorms and often causing severe floods (Fu et al. 2022; Sun et al. 2019; Wu et al. 2011; Zhao et al., 2008). During the DBRS of 2022, South China experienced a record-breaking extreme rainfall event (Cheng et al. 2023). Characterized by a broad rainfall coverage with scattered regional heavy rainfall centers, the extreme rainfall event caused widespread floods and consequent geological hazards and attracted much attention (Cheng et al. 2023; Sheng et al. 2023; Meng and Yu 2022).

The mesoscale convective system (MCS) plays an especially important role in warm season rainfall (Feng et al., 2019; Houze 2004; Zheng et al. 2013) and long-lasting

MCSs are responsible for majority of extreme rainfall events (Chen et al. 2022; Feng et al. 2019; Guo et al. 2022; Luo et al. 2013; Punkka and Bister 2015; Schumacher and Johnson 2005; Zhang et al. 2022). On satellite infrared images, MCSs often appear as cold-cloud shields (CCSs) with a certain temporal and spatial scale and can be identified using the criteria of brightness temperature, cloud extend and life duration (Guo et al. 2022; Mai et al. 2021; Meng et al. 2020; Yang et al. 2015, 2020). The initiation, formation and development of MCSs are highly influenced by large-scale circulations (Feng et al. 2019; Peters and Schumacher 2014; Salio et al. 2007; Song et al. 2019). Synoptic systems such as upper-level troughs (Liu et al. 2020; Mai et al. 2021; Peters and Schumacher 2014; Wu et al. 2019; Yang et al. 2020), low-level vortices/shear lines (Qian et al. 2020), fronts (Qian et al. 2021) and low-level jets (LLJs) (Du and Chen 2019; Trier and Parsons 1993) are found favorable for the generation of MCSs. The divergence and quasi-geostrophic ascent ahead of the upper-level troughs contributes to MCSs' formation (Liu et al. 2020; Mai et al. 2021; Wu et al. 2019; Yang et al. 2020). The MCSs tend to occur near the entrance region of an upper-level jet in warm seasons in the United States (Peters and Schumacher 2014). The LLJs establish instability and produce low-level convergence, which is also essential for the initiation and development of MCSs (Du and Chen 2019; Trier and Parsons 1993). The enhancement of moisture in the low troposphere favors the developments of MCSs (Bretherton et al. 2004; Kuo et al. 2017).

From the perspectives of both operational practice and scientific research, it is imperative to understand the controlling physical mechanism responsible for the extreme rainfall during the DBRS of 2022. Although several studies have investigated the extreme rainfall event from the perspective of moisture and energy budget (Cheng et al. 2023; Sheng et al. 2023), due to the lack of comprehensive analysis, some scientific issues remain unsolved: (a) How to quantitatively describe the severity of the extreme rainfall during DBRS of 2022? (b) What is the configuration of the weather systems and how do they contribute to the extreme rainfall from the synoptic-scale perspective? (c) As MCSs are directly rainfall-producing systems, to what extent are MCSs responsible for the extreme rainfall? (d) Where do these MCSs originate and what are the environmental conditions favorable for their formation? The present study aims to address these questions and the remainder of this paper is organized as follows. Section 2 introduces the data and methodologies. Section 3 presents the general characteristics of the rainfall during the DBRS of 2022. In Section 4, through the inspection of synoptic systems and a case study, the configuration of systems and their contribution to the extreme rainfall are investigated. Section 5 presents the features of the MCSs and the environmental conditions favorable for their formation. Finally, a summary is given in Section 6.

2 Data and methodology

The typical DBRS is defined as a period from 21 May to 20 June each year in most studies (Wu et al. 2017; Qian et al. 2020). However, for the present study, the DBRS is defined from 21 May to 21 June instead. This is because the final rainfall event over South China during the DBRS of 2022 continued until 21 June (Meng and Yu 2022).

Hourly rainfall records of both national and regional rain gauge stations over South China (104° – 118° E, 18° – 27° N) provided by China Meteorological Administration are used in the present study. The data collected from 8927 regional stations is utilized to analyze details of precipitation during the DBRS of 2022. Only data from 347 national stations covering from 1981 to 2022 is utilized to compare rainfall during the DBRS of 2022 with climatology, for the time span of the data from national stations is much longer than that from regional stations. The analysis of synoptic circulations and calculation of environmental parameters are based on the fifth-generation ECMWF (European Centre for Medium Range Forecasts) reanalysis (ERA5) data, with a temporal resolution of 1 h and a spatial resolution of 0.25° (Hersbach et al. 2020). The brightness temperature (BT) at the $10.8\text{ }\mu\text{m}$ band of the Advanced Geosynchronous Radiation Imager onboard the Fengyun-4A (FY-4A) satellite is utilized to identify and track the MCS. The spatial resolution of FY-4A BT data is 4 km at the nadir. The temporal resolution of regional observations over China and its surrounding area is ~ 5 min (Yang et al. 2017).

Two indicators, namely the mean hourly rain rate and the rainfall frequency, are utilized to quantitatively describe the features of the rainfall during the DBRS of 2022. The rainfall frequency refers to the total number of hours with rainfall ≥ 0.1 mm in a certain period, and the mean hourly rain rate is obtained by dividing the total rainfall amount by the rainfall frequency.

The criteria and steps used in the present study to identify MCS are outlined as follows (Yang et al. 2020): 1) detect CCSs with temperature $\leq -52^{\circ}\text{C}$ and extent $\geq 5000\text{ km}^2$ in the BT fields; 2) track CCSs at different time steps; and 3) continuous CCSs that last longer than 3 h are identified as MCSs. The first time that an MCS satisfies the above criteria is considered to be MCS formation.

In order to accurately track CCSs, the optical flow between two successive BT fields are calculated first. The target CCS at the previous time will be extrapolated by adding the optical flow and compared with all CCSs at the later time. The CCS with an overlapping rate $\geq 30\%$ is considered the successor of the target CCS.

The rainfall is matched with MCS by the method proposed by Ai et al. (2016) in the present study. For a given

MCS, at each time step, its boundary corresponds to an approximate rectangle on the BT field, and the scope of the circumscribed circle associated with this rectangle is regarded as the MCS-influencing area, within which the rainfall is considered to be associated with the MCS.

3 Features of rainfall during the DBRS of 2022

3.1 The general features

During the DBRS of 2022, the large values of total rainfall amount in South China are mainly located over northeastern Guangxi (GX) and northern Guangdong (GD) (Fig. 1b). The maximum cumulative rainfall of 1572.6 mm occurs at a regional station in Guilin, GX (the geographical distribution of provinces and cities mentioned in the text is shown in Fig. 1a). The large values of mean hourly rain rate (Fig. 1c) are mainly located over two regions: the coastal areas that include southwestern GD, southeastern GX, and northern Hainan, and the mountainous areas in northern GD and northern GX. The large values of rainfall frequency (Fig. 1d) occur over northeastern GX, northern GD and southwestern Fujian. The hourly rain rates recorded by stations in northeastern GX and northern GD are typically over 3 mm h^{-1} , and with rainfall frequency exceeding 300 h, these two regions suffered the largest total rainfall amount.

Previous studies suggest that the maximum values of rainfall during pre-summer rainy season over South China are primarily located in 5 regions (Fig. 1a), namely Yangjiang in southwestern GD, Shanwei in southeastern GD, Guangzhou in central GD, Fangchenggang in southern GX, and Liuzhou in northeastern GX (Li and Du 2021; Liu et al. 2019; Xia et al. 2006; Sun and Zhao 2000; Bao 2007). However, during the DBRS of 2022, both the values of the total rainfall amount and the rainfall frequency are relatively small over the southern part of South China, indicating that the rainfall during the DBRS of 2022 is different from climatology.

Statistics of daily rainfall during the DBRS of 2022 are shown in Fig. 1e. The maximum of regional mean of daily rainfall over entire South China occurred on June 13 with the value of 27.8 mm. The maximum of medians and interquartile ranges also appeared on June 13, with the value of 16.1 mm and 39.6 mm, respectively. Note that there are 4 days when the median of daily rainfall exceeded 10 mm, namely May 22, May 23, June 11 and June 13, indicating that on the 4 days over a half of all stations in South China experienced moderate rain (10 mm d^{-1} for operational observation in China).

3.2 Comparison with climatology

To further investigate the rainfall features during the DBRS of 2022, 347 national stations with complete hourly rainfall records from 1981 to 2022 are utilized to compare the rainfall during DBRS of 2022 with climatology. The mean values of total rainfall amount of 347 national stations during the DBRS of each year from 1981 to 2022 are shown in Fig. 2a. The rainfall amount during the DBRS of 2022 is the highest since 1981, surpassing the well-known DBRS heavy rainfall events in 1998, 2005 and 2008 (Mu et al. 2008; Wang et al., 2011; Chen and Zhao 2004). The climatological value calculated based on the rainfall amount from 1991 to 2020 is 277.9 mm, while the rainfall amount during the DBRS of 2022 is 441.6 mm, 59% more than the climatology. The rainfall anomalies of 347 national stations are shown on Fig. 2b. Positive anomalies are found at 302 out of 347 stations, including 66 (11) stations with anomalies extent of 100% (200%), with the maximum anomaly of 282.2%. The rankings of the rainfall amount during the DBRS of 2022 compared to the rainfall amount during the DBRSs from 1981 to 2022 are shown in Fig. 2c. Of the 347 stations, 247 are ranked in the top 10 and 70 stations are ranked the first. The stations with rainfall anomalies exceeding 100% or ranked the first are mainly located over northeastern GX and northern GD, consistent with the area with the highest values of total rainfall amount.

In conclusion, the record-breaking extreme rainfall event during the DBRS of 2022 is characterized by the highest rainfall amount in history, higher hourly rain rate and rainfall frequency than climatology, and an abnormal spatial distribution with much higher (lower) rainfall amount in the northern (southern) part of South China and caused widespread floods and consequent geological hazards (Meng and Yu 2022).

4 Synoptic circulations

The above statistics show that during the DBRS of 2022, total rainfall amount, rainfall frequency and short-term heavy rain frequency over South China exceed the climatology. In order to explore the causes for the extreme rainfall during the DBRS of 2022 from the perspective of the synoptic scale, the configuration of weather systems and their contribution to the rainfall are analyzed in this section.

To evaluate the ability of the ERA5 data on capturing the synoptic circulations, the accumulative precipitation from the ERA5 data (Fig. 3b) is compared with the observation (Fig. 3a). The ERA5 data not only exhibits a similar spatial distribution of accumulative precipitation compared with the observation, but also accurately captures the three precipitation centers in the northern part of South China. With

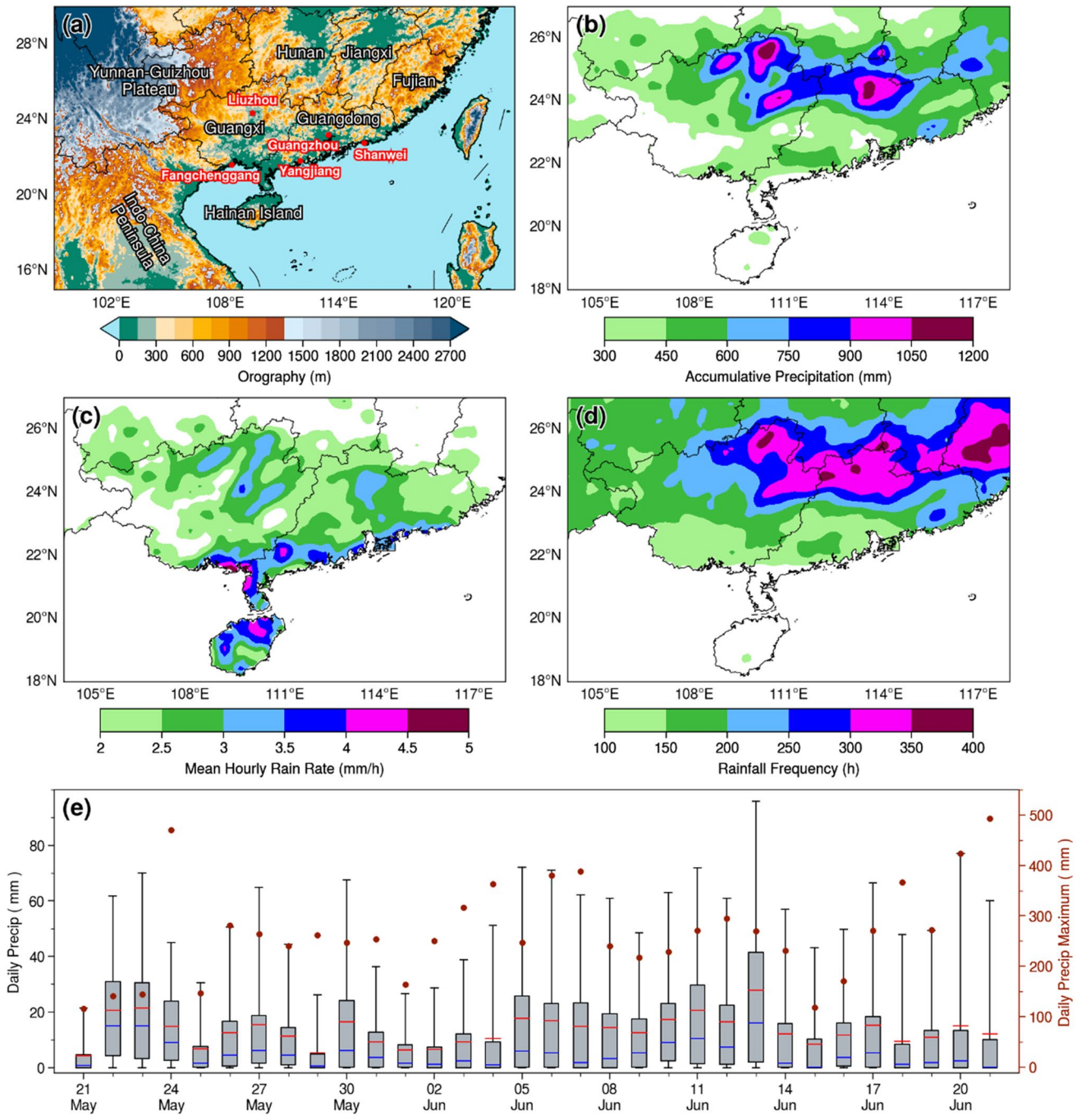


Fig. 1 Distribution of the orography over South China (a), total rainfall amount (b; unit: mm), mean hourly rain rate (c; unit: mm h^{-1}), rainfall frequency (d; unit: h) and statistics of daily rainfall (e; unit: mm) during the DBRS of 2022. The 5 climatological rainy centers are marked in red dots in (a). The top and bottom edges of boxes

(caps of whiskers) in (e) indicate the 75th and 25th (95th and 5th) percentiles, respectively, the blue (red) dashed line indicate the median (mean) values and the red dots indicate the maximum rainfall of each day, corresponding to y-axis on the right side

a correlation coefficient of 0.75 between the accumulative precipitation of the two datasets, it can be assumed that the ERA5 data can well reflect the real state of the atmosphere.

The mean circulation pattern at 500 hPa (Fig. 3c) consists of a ridge-trough couplet with the ridge over western

Mongolia and the trough over northeastern China characterized by positive and negative geopotential height anomaly centers, respectively, which indicates that most of the northern and central China has cold air flowing down from high latitude. In the low latitude, the western Pacific subtropical

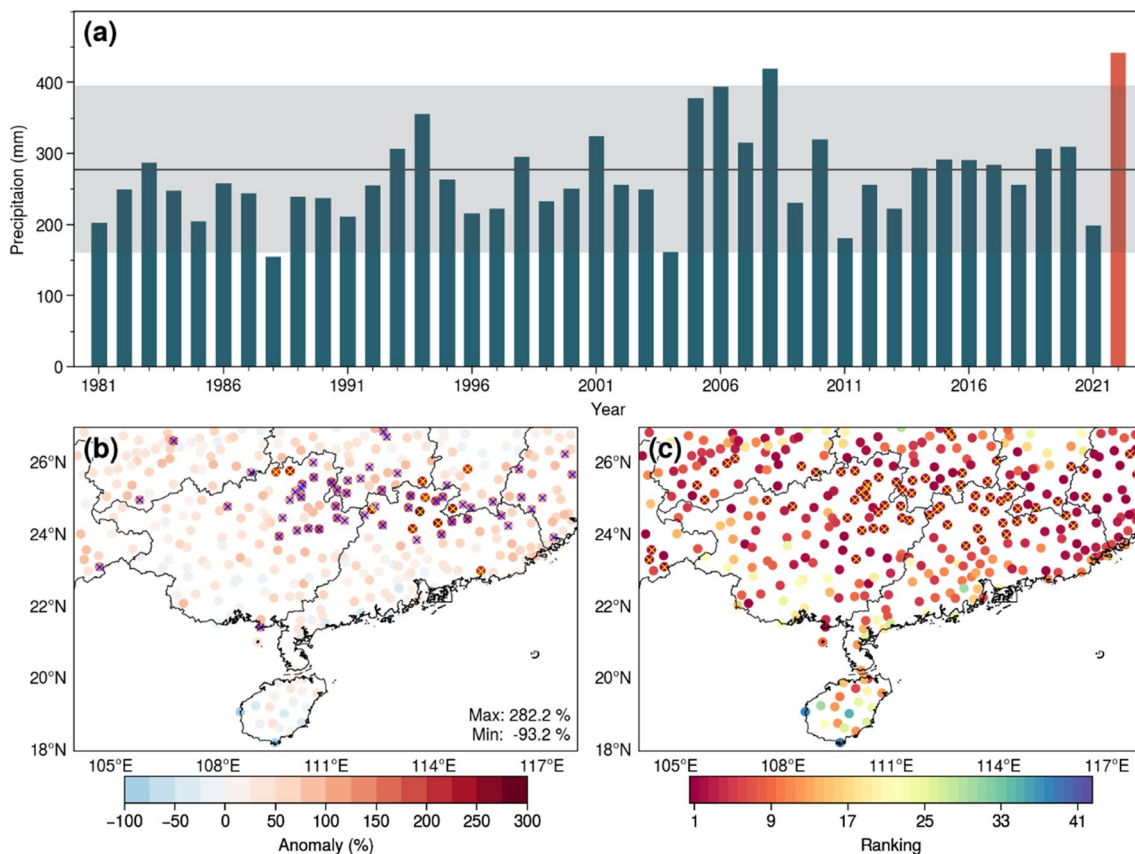


Fig. 2 The mean values of total rainfall amount during the DBRS from 1981 to 2022 (a; unit: mm), the anomaly extent of rainfall amount during the DBRS of 2022 comparing to climatology (b; unit: %) and the rankings of rainfall amount in history since 1981 (c). The grey line in (a) indicates the climatological mean and the light grey

shading indicates three times of standard deviation. The stations with anomaly $\geq 100\%$ ($\geq 200\%$) are marked in blue (yellow) crosses in (b). The yellow crosses in (c) indicate that these stations rank top in history

high is stronger than climatology with a positive geopotential height anomaly and there are two troughs over Bay of Bengal and Indo-China Peninsula, respectively. Note that an extensive negative geopotential height anomaly covers over South China and its west, which is due to the continuous eastward propagation of the short-wave troughs (Table 1). The cyclonic differential vorticity advection ahead of the short-wave troughs is favorable for the developments of vortices or cyclones. The mean southwesterly flows are strong at lower level, which on the one hand continuously transport moisture from the tropical ocean and on the other hand encounters with the cold air from the high latitude, forming a frontal zone and providing large-scale convergence for the rainfall during the DBRS of 2022.

The anomalies of the moisture flux field and the equivalent potential temperature field at 850 hPa (Fig. 3 d) are calculated to analyze the thermodynamic effects on the extreme rainfall during the DBRS of 2022. The moisture transportation is much stronger during the DBRS of 2022 than that of climatology, with two main transportation paths,

namely the one from South China Sea and the one from Beibu Gulf, both showing abnormal southerly components of the moisture flux. The moisture significantly converges at the northern part of South China. Over the northern part of South China, the evident positive anomaly centers of the equivalent potential temperature field suggest a favorable environment for convection and precipitation. The abnormality of the thermodynamic conditions not only explains the extreme precipitation during the DBRS of 2022, but also explains why the extreme precipitation mainly occurs over the northern part of South China.

Through subjective identification of the daily weather maps, it is found that the short-wave troughs, LLJs, shear lines or vortices, and fronts are mainly responsible for the rainfall during the DBRS of 2022 (Table 1). The previous studies suggest that the above mentioned synoptic systems, together with the land-sea contrast and the mountain-plain topography, are closely related to extreme rainfall events over South China (Du et al. 2014; Wu et al. 2020). To further illustrate the configurations and effects on the rainfall

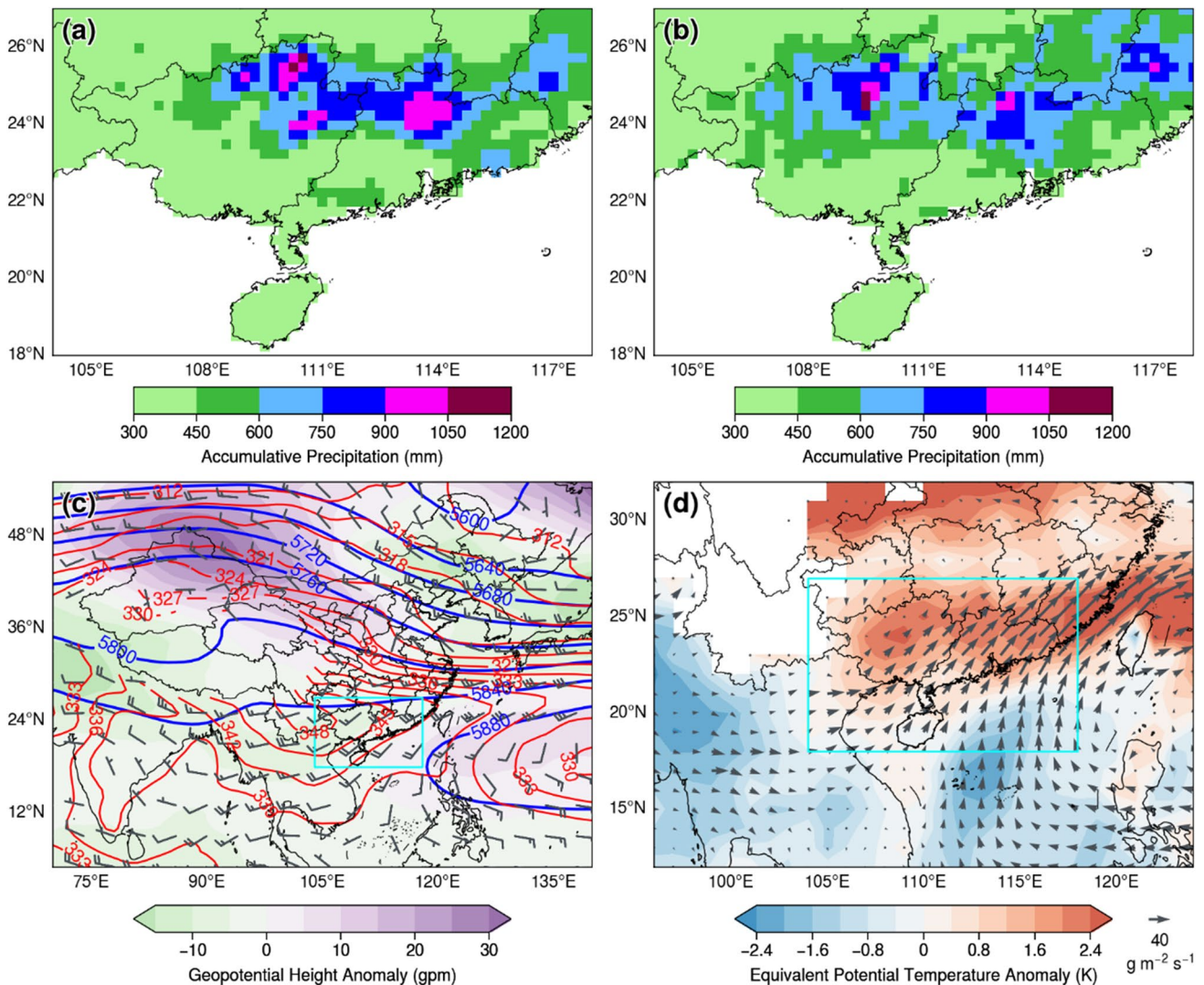


Fig. 3 The accumulative precipitation from the observations (a, interpolated to 0.25°) and the ERA5 data (b) and the mean circulation patterns (c and d) during the DBRS of 2022. The blue and red contours in (c) represent the mean geopotential height (unit: gpm) at 500 hPa and the mean equivalent potential temperature (unit: K) at 700 hPa during the DBRS of 2022, respectively. The shading in (c) represents the geopotential height anomaly (unit: gpm) and the wind barbs rep-

of the above-mentioned systems, a case study is conducted in the following part. The rainfall distribution, synoptic circulations and corresponding cross-section on June 13, the day with the maximum rainfall amount during the DBRS of 2022, are shown on Fig. 4. Daily rainfall distribution on June 13 (Fig. 4a) show that a rainfall belt with several maximum center positions over the northern part of South China, exhibiting similar distribution compared to the total rainfall distribution during the entire DBRS of 2022.

A deep cyclonic flow, characterized by shear lines, is located over western GX and Yunnan, tilting westward with height (Fig. 4 b, c and d). The rainfall mostly occurs ahead

represent the mean wind field (unit: m s^{-1}). The vectors and shadings in (d) represent the moisture flux anomaly (unit: $\text{g m}^{-2} \text{s}^{-1}$) and the equivalent potential temperature anomaly (unit: K), respectively. For the wind barbs, the half barb represents 2 m s^{-1} and the full barb represents 4 m s^{-1} . The cyan dashed rectangle in (c) and (d) indicates the region of South China

of the cyclonic flow. The cross section along 114°E (Fig. 4 e) over the rainfall maximum shows that the wind direction shifts clockwise with height over $23^\circ\text{--}25^\circ\text{ N}$ (south-southwest at 950 hPa, southwest at 850–700 hPa and west at 600 hPa), indicating the existence of the deep warm advection, which provides quasi-geostrophic ascent and is favorable for convection initiation and rainfall producing (Reif and Bluestein 2017). The frontal zone is located over the northern part of South China (Fig. 4 c and d). The cross section shows that the isotherms of the equivalent potential temperature extend upwards and northwards over $25^\circ\text{--}27^\circ\text{ N}$, suggesting that frontal forcing combined with orographic

Table 1 The major synoptic systems affecting South China during the DBRS of 2022

	500 hPa	850 hPa
21 May		
22 May		LLJ, shear line
23 May		LLJ, shear line
24 May		
25 May	Cyclonic flow	Shear line
26 May	Trough	Shear line
27 May	Trough	LLJ, shear line
28 May		LLJ
29 May		LLJ, shear line
30 May	Trough	Shear line, front
31 May		
1 June		LLJ
2 June		LLJ
3 June	Trough	LLJ
4 June	Trough	LLJ
5 June	Trough	LLJ, shear line, front
6 June	Trough	Shear line, front
7 June	Trough	Shear line, front
8 June	Trough	LLJ, vortex
9 June	Trough	LLJ, vortex, front
10 June	Vortex	Vortex, front
11 June	Vortex	LLJ, vortex, front
12 June	Cyclonic flow	LLJ, shear line
13 June	Cyclonic flow	LLJ, shear line, front
14 June		LLJ, shear line, front
15 June		LLJ, shear line, front
16 June	Cyclonic flow	LLJ, shear line, front
17 June		LLJ
18 June	Trough	LLJ
19 June	Trough	LLJ
20 June	Trough	LLJ
21 June	Trough	LLJ

* The flow with wind speed $\geq 12 \text{ m s}^{-1}$ and v-component > 0 is identified as the LLJ

lifting forces the warm-moist air mass ascending. At the exit of the LLJ, the convergence of the southwesterly flow and the northerly flow provides synoptic-scale ascent (Fig. 4 c and d). Such kind of synoptic-scale convergence and ascent is favorable for the initiation of convective cells and the subsequent organization into the MCS from them (Maurer et al. 2017). In addition, on the cross section, the equivalent potential temperature decreases with height over the region south of 27° N , suggesting the existence of an extensive and deep convective instability, creating favorable environmental conditions for the heavy rainfall. Under the configuration of above-mentioned systems and orographic effects, an intense synoptic-scale ascent with maximum vertical

velocity $\geq 0.5 \text{ m s}^{-1}$ occurs at the exit of the LLJ and south of the frontal zone (Fig. 4 e), causing the heavy rainfall on June 13. Similar configurations impact South China repetitively during the DBRS of 2022, causing multiple heavy rainfall events, leading to the extreme rainfall (Table 1).

Characteristics and environmental conditions of MCSs during the DBRS of 2022.

4.1 Characteristics of the MCSs

The previous studies have pointed out that the MCS is the direct producer of the heavy rainfall (Ai et al. 2016; Ninomiya et al. 1981; Mai et al. 2020). To further investigate the extent to which the MCSs account for the rainfall during the DBRS of 2022, and explore the environmental conditions favorable for their formation, 165 MCSs are identified and tracked based on the BT field at the $10.8 \mu\text{m}$ band from the FY-4A satellite. Then hourly rainfall at all stations over South China is matched with the MCSs and the proportion of the MCS-related rainfall to the total rainfall at each station is calculated (Fig. 5). The general result shows that during the DBRS of 2022, 54.35% of total rainfall is related to the MCSs (Fig. 5 b). For the rainfall amount with hourly rate $\geq 20 \text{ mm}$ ($\geq 50 \text{ mm}$), the proportion is 75.93% (83.62%). The spatial distribution (Fig. 5a) shows that the proportions over northern and northeastern GX, central and southern GD and northern Hainan are higher than 70%.

Five regions are selected based on the local maximum of MCS formation as shown on the two-dimensional histogram in Fig. 6a, namely the Yunnan-Guizhou Plateau (YGP), the northeastern Indo-China Peninsula, the Hainan Island, the mountains over northeastern GX and northern GD (MT) and the coastal areas over southern GD (CS), to further investigate the MCS activities and the environmental conditions favorable for MCS formation. The five high occurrence region are consistent with the results derived from radar detections by Chen et al. (2022). The MCSs forming over the northeastern Indo-China Peninsula mostly propagate westwards, thus the rainfall over South China during the DBRS of 2022 is mainly caused by the MCSs originating from the other 4 regions.

The trajectory (i.e., the longitude/latitude series) of an MCS's centroids can be regarded as a function of its life cycle. By interpolating the longitude/latitude series to the fixed points of life cycle (i.e., 1%, 2%, 3%, ..., 100%), a life-cycle based trajectory with a fixed length can be obtained. Composite trajectories of the MCSs from the 4 different regions (Fig. 6b) indicates that the MCSs from YGP mainly propagate southeastward with the longest path, consistent with the previous studies (Chen et al. 2022; Xia et al. 2006). The MCSs from MT and CS mostly propagate eastwards and the MCSs from Hainan Island are quasi-stationary.

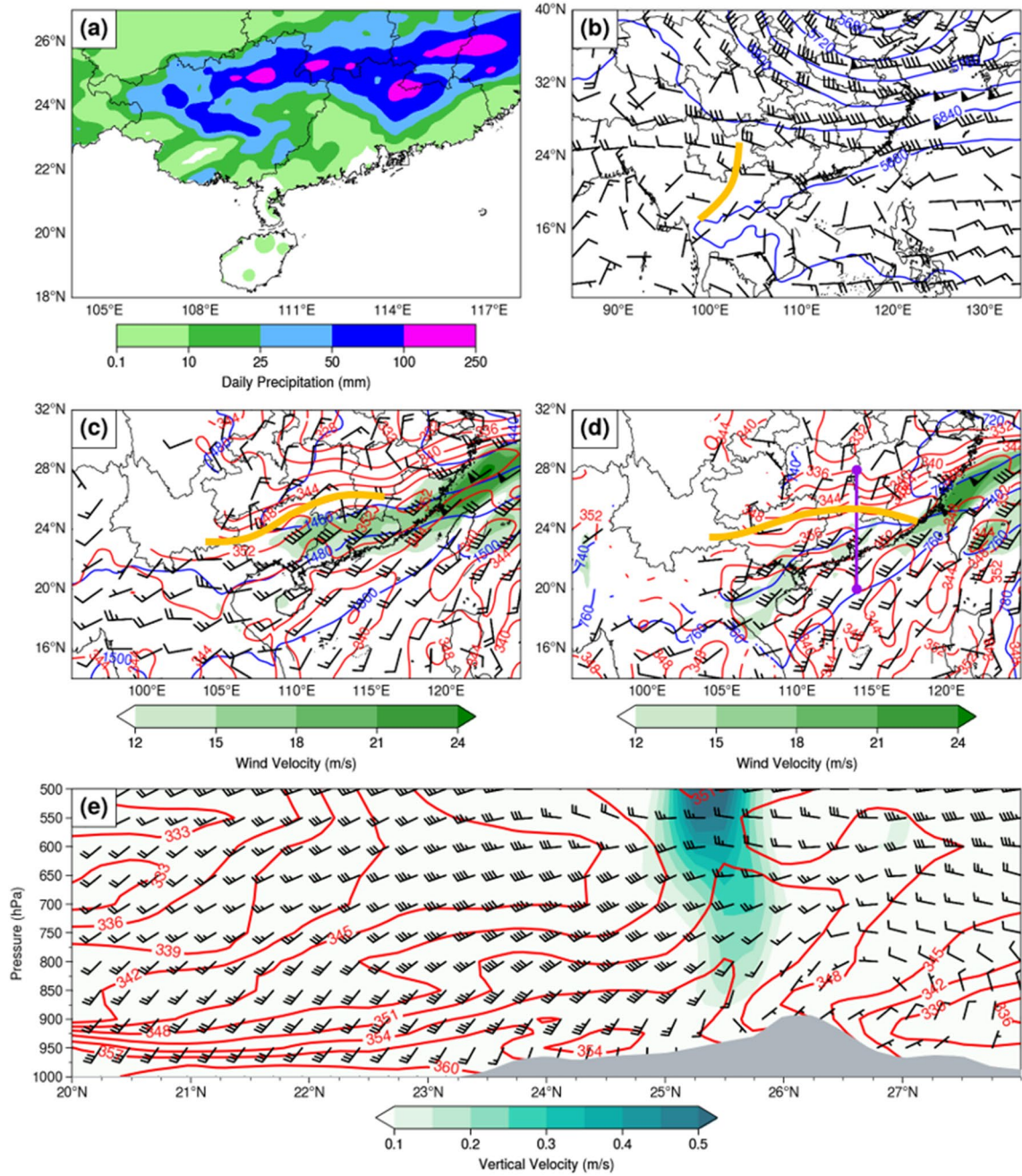


Fig. 4 The daily rainfall on June 13, 2022 (a), synoptic circulations at 500 hPa (b), 850 hPa (c), 925 hPa (d) and cross section over 114°E on June 13 0800 BST, 2022 (e). The blue contours in (b), (c) and (d) represent the geopotential height (unit: gpm), the red contours represent the equivalent potential temperature (unit: K) and the wind barbs represent the wind field (unit: m s^{-1}). For the wind barbs, the half

barb represents 2 m s^{-1} , the full barb represents 4 m s^{-1} and triangle represents 20 m s^{-1} . The colored shadings in (c) and (d) indicate that the wind speed $\geq 12 \text{ m s}^{-1}$. The colored shading in (e) represents that the vertical velocity $\geq 0.1 \text{ m s}^{-1}$, and grey area indicates the orography. The yellow lines represent trough at 500 hPa or shear lines at 850/925 hPa

The MCS coverage is calculated by adding up the hourly coverages of the CCSs over the entire lifetime of the MCS. The total coverages of all MCSs from the four different regions are shown on Fig. 7. The total coverage of the 28 MCSs from YGP (Fig. 7a) shows that the high value center is located over northern GX and northern

GD, which is basically the same as the distribution of total rainfall (Fig. 1b). The total coverage of the 19 MCSs from Hainan Island (Fig. 7b), with the maximum value over 100, is mainly limited over the Hainan Island. The total coverage of the 25 MCSs from MT (Fig. 7c), with the maximum value of 60 located over northeastern GD, may account for

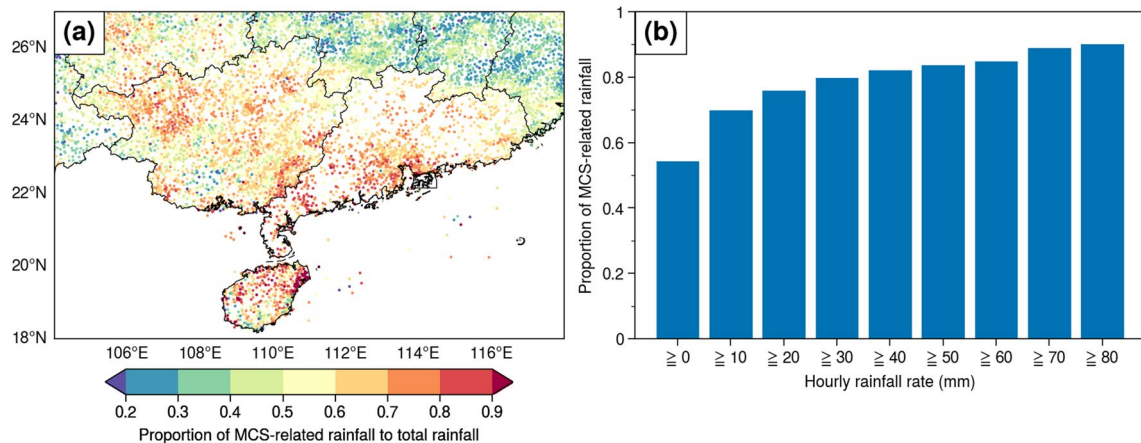


Fig. 5 The proportion of MCS-related rainfall to total rainfall at each station (a) and of different hourly rain rate grades (b) during the DBRS of 2022

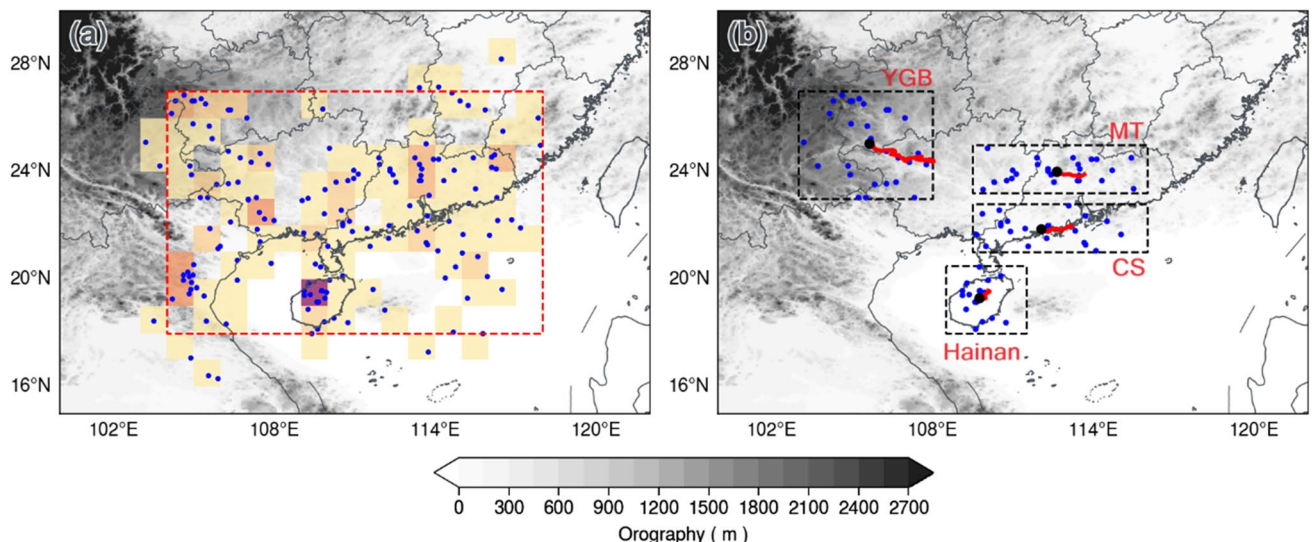


Fig. 6 A(a) The formation locations of MCSs (blue dots) and corresponding two-dimensional histogram (colored shading). The red dashed rectangle indicates the region of South China. (b) The for-

mation locations (blue dots) and composite trajectories (red lines) of MCSs from 4 regions (black dashed rectangle). The grey shading represents terrain height (unit: m)

the rainfall over this region. The total coverage of the 20 MCSs from CS, with the maximum value centers located over the coast and the ocean, may be related to the rainfall over southern GD.

The comparison between the MCSs from MT and CS indicates that although the amounts, propagation direction and length are approximately the same, the total coverage differs from each other. The statistics in Table 2 also suggest that the MCSs from MT are featured by smaller scale, shorter lifetime and faster propagation. Table 1 shows that low level shear lines are quite active over the northern part of South China, and Sun and Zhao (2002) found that the rainfall caused by the convective systems around shear lines

over South China has a lifetime of 3 h, which is the same as the lifetime of the MCSs from MT, suggesting that the MCSs from MT may be related to the shear lines. The MCSs from CS are featured by larger scale, longer lifetime and slower propagation, suggesting that their formations may be related to the interaction between the LLJs and the land-sea topography (Xia et al. 2006).

The diurnal variations of formation time of the MCSs from 4 different regions are shown on Fig. 8. The MCSs from YGP tend to form in the afternoon and early evening (Fig. 8a), with 61% of them form during 1400–2000 BST (Beijing Standard Time). The MCSs from Hainan Island mostly form in the afternoon (Fig. 8b), with 58%

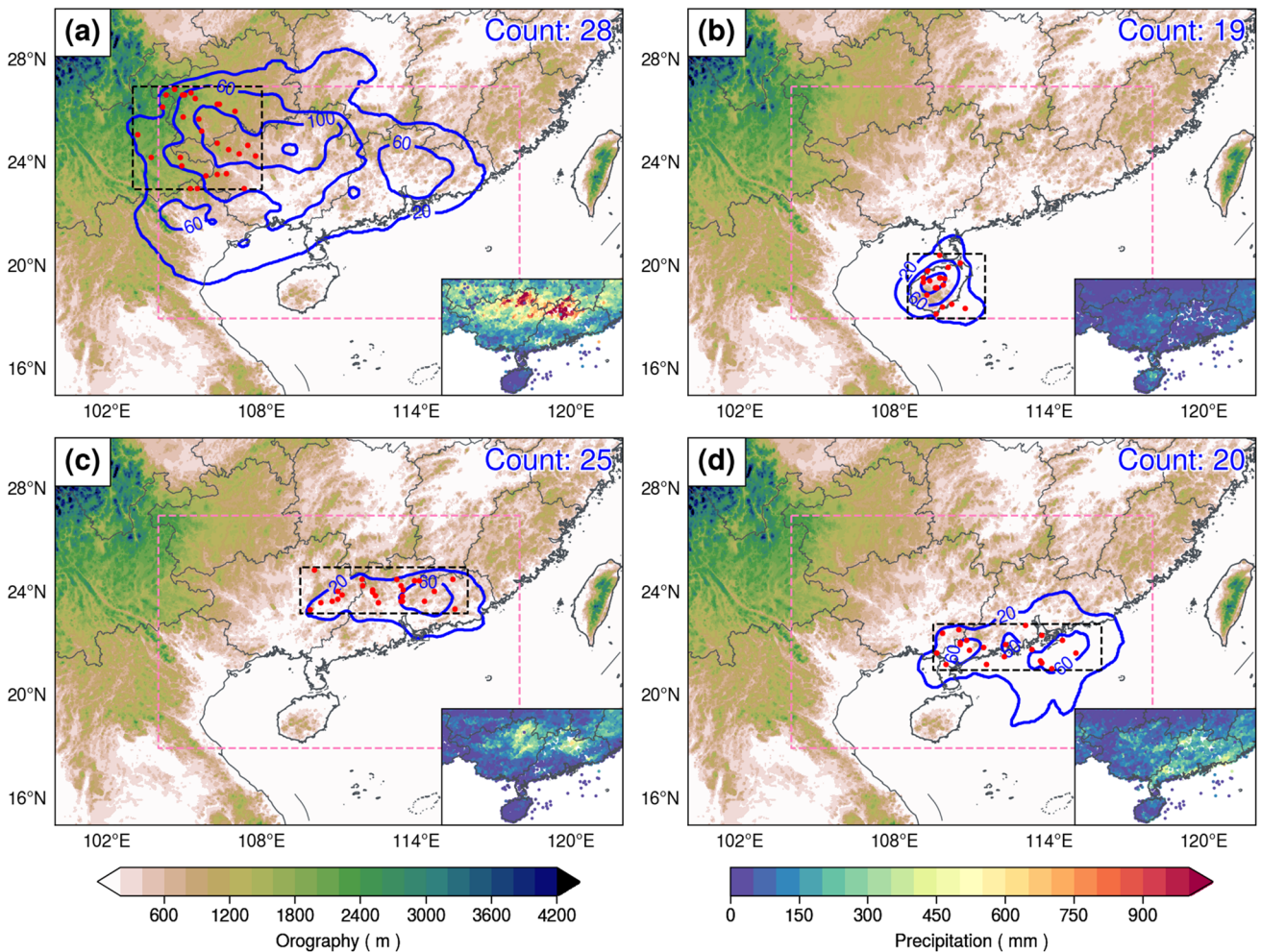


Fig. 7 The total coverages (blue contours) of MCSs from YGP (a), Hainan Island (b), MT (c) and CS (d). The colored shadings represent terrain height (unit: m). Subplots on the right-bottom corner show total rainfall amount over South China during the lifetimes of MCSs (unit: mm)

in 1400–1700 BST. The MCSs from MT has two formation peaks, namely 1400–1700 BST and 0200–0500 BST, accounting for 32% and 24% respectively (Fig. 8c). The formation of MCSs from CS peaks in the early morning (Fig. 8 d), with 30% in 0200–0500 BST.

4.2 Environmental conditions for MCS formation

The composite analysis of circulations and environmental conditions 3 h before MCS formation is conducted to further explore the causes of MCSs from the synoptic perspective. Composite circulations show that the MCSs from 4 regions all tend to form ahead of mid-level troughs at 700 hPa (Fig. 9).

Over YGP, the MCSs form in the large-scale warm moist air mass, with a high value center of the equivalent potential temperature exceeding 356 K at 850 hPa (Fig. 9b). The vertical profile of the equivalent potential temperature (Fig. 10e) indicates the existence of the deep and strong convective instability, with the depth of 4.28 km (above grand level) and the lapse rate of -4.58 K km^{-1} . The LLJ at 850 hPa (Fig. 9b) provides convergence at the exit and transport moisture. The wind direction shifts clockwise with height on the vertical profile (Fig. 10a) suggesting a warm air advection. A simple conceptual model emerges from above mentioned analysis:

Table 2 The mean value of lifetime, extend and propagation speed of the MCSs from 4 different regions

	Lifetime (h)	Extend Area (km^2)	Propagation Speed (km h^{-1})
YPG	16.36	6.87	15.18
Hainan Island	5.49	4.66	7.93
MT	5.73	3.0	18.26
CS	8.75	6.04	13.01

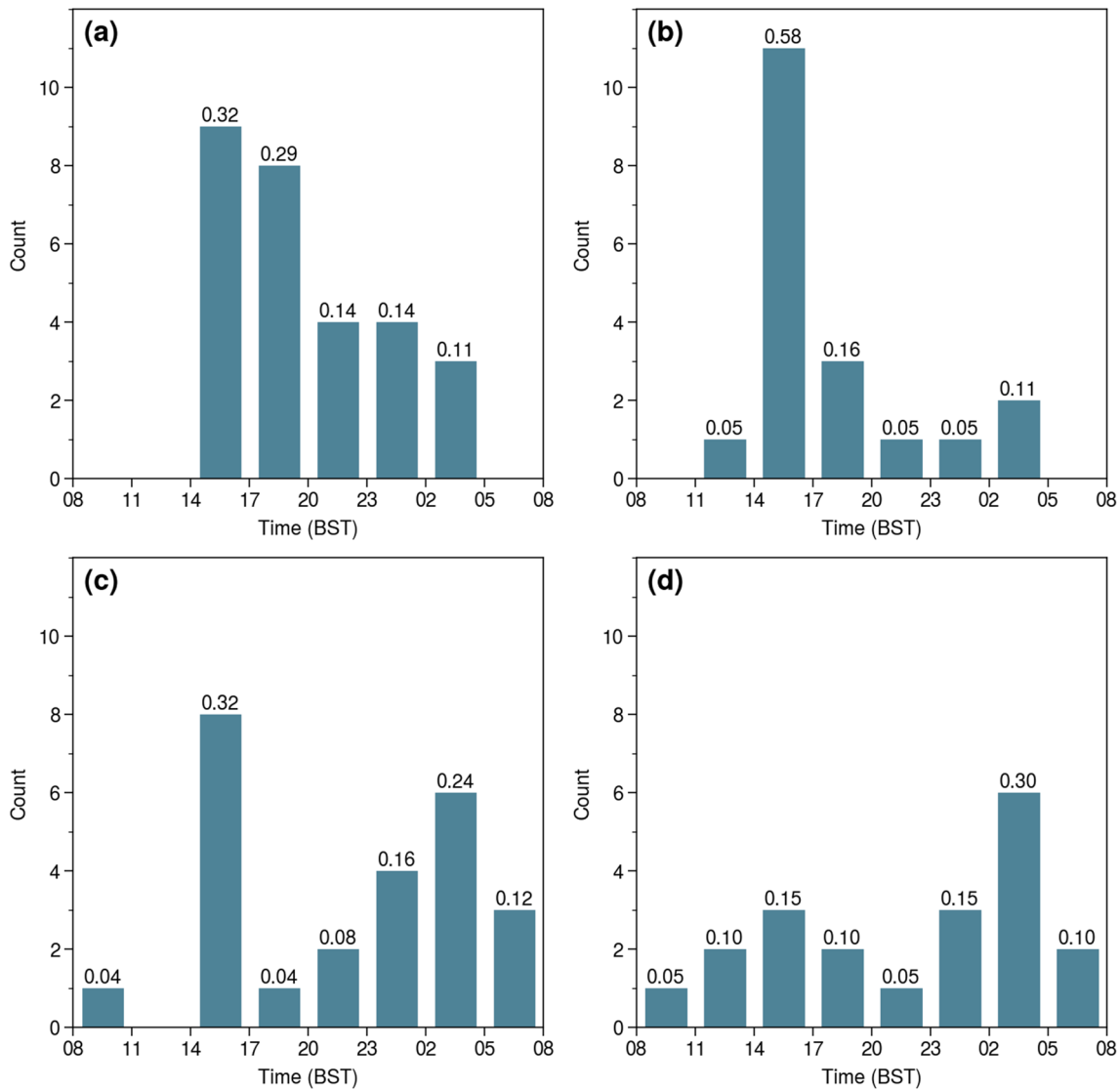


Fig. 8 The diurnal variations of MCSs' formation over YGP (a), Hainan Island (b), MT (c) and CS (d). The numbers over the bars represent the proportion of MCSs forming in different time grades to the total amount of MCSs in corresponding region

the large-scale warm and moist air mass provides the instability for the convection; the deep warm air advection causes the quasi-geostrophic ascent as the possible initiation mechanism of the convection; with the large-scale convergence, small convective systems are organized/or developed into large MCS, causing the heavy rainfall.

Before the formation of MCS over Hainan Island, the southwesterly flow transports moisture from the Indo-China Peninsula, leading to the moistening over Hainan Island (Fig. 9d). T-InP plot (Fig. 10b) shows that the surface temperature on Hainan Island is higher compared to the other 3 regions, mainly caused by the diabatic heating in the afternoon. The surface diabatic heating combined with the low-level moistening causes the increase of the equivalent potential temperature, leading to the contrasting of the equivalent

potential temperature between the low level and the middle level, with the largest lapse rate of -6.14 K km^{-1} (Fig. 10f) and the highest convective available potential energy (CAPE) of 3364.3 J kg^{-1} (Fig. 10b). The diurnal thermal heating plays an important role in convection initiation on Hainan Island (Zhu et al. 2021), that is why the MCSs from Hainan Island tend to form in the afternoon.

The remarkable feature of circulation favorable for MCS formation over MT and CS is the existence of the LLJ (Fig. 9e and g). The strong LLJ transports moisture from the Bay of Bengal and the South China Sea, creating favorable environments for MCS formation over MT and CS with the precipitable water $\geq 60 \text{ mm}$ and surface dew-points $\geq 25^\circ\text{C}$ (Fig. 10c and d). The abundant moisture supply produces strong convective instability, and the high dew-point leads to low lifting

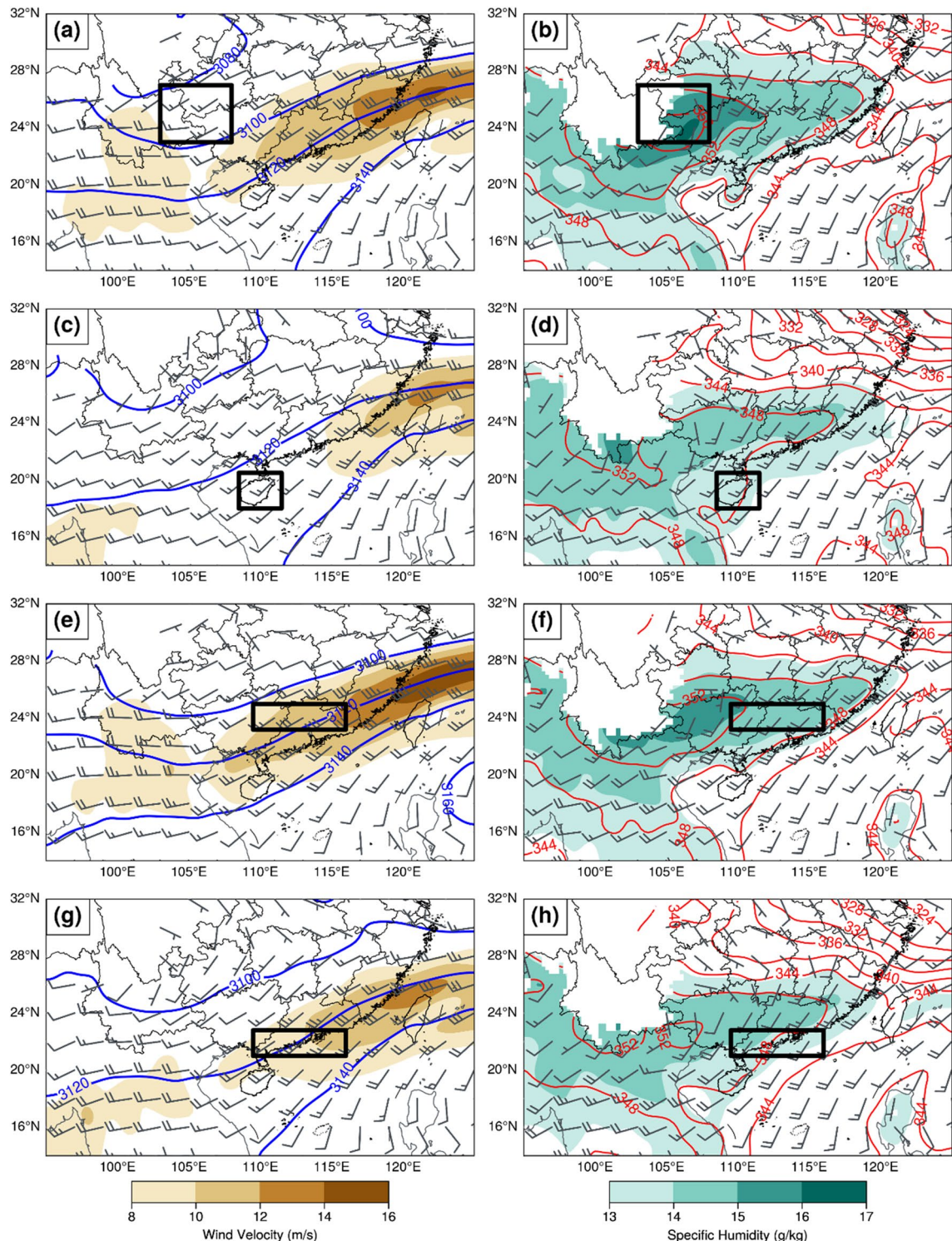


Fig. 9 The composite circulations 3 h before MCSs' formations at 700 hPa (left columns), 850 hPa (right columns) over YGP (a, b), Hainan Island (c, d), MT (e, f) and CS (g, h). The blue contours represent the geopotential height (unit: gpm), the red contours represent the equivalent potential temperature (unit: K) and the wind barbs rep-

resent the wind field (unit: m s^{-1}). For the wind barbs, a half barb represents 2 m s^{-1} , a full barb represents 4 m s^{-1} and a triangle represents 20 m s^{-1} . The orange (green) shadings at 700 (850) hPa indicate that the wind speed $\geq 12 \text{ m s}^{-1}$ (the specific humidity $\geq 12 \text{ g kg}^{-1}$)

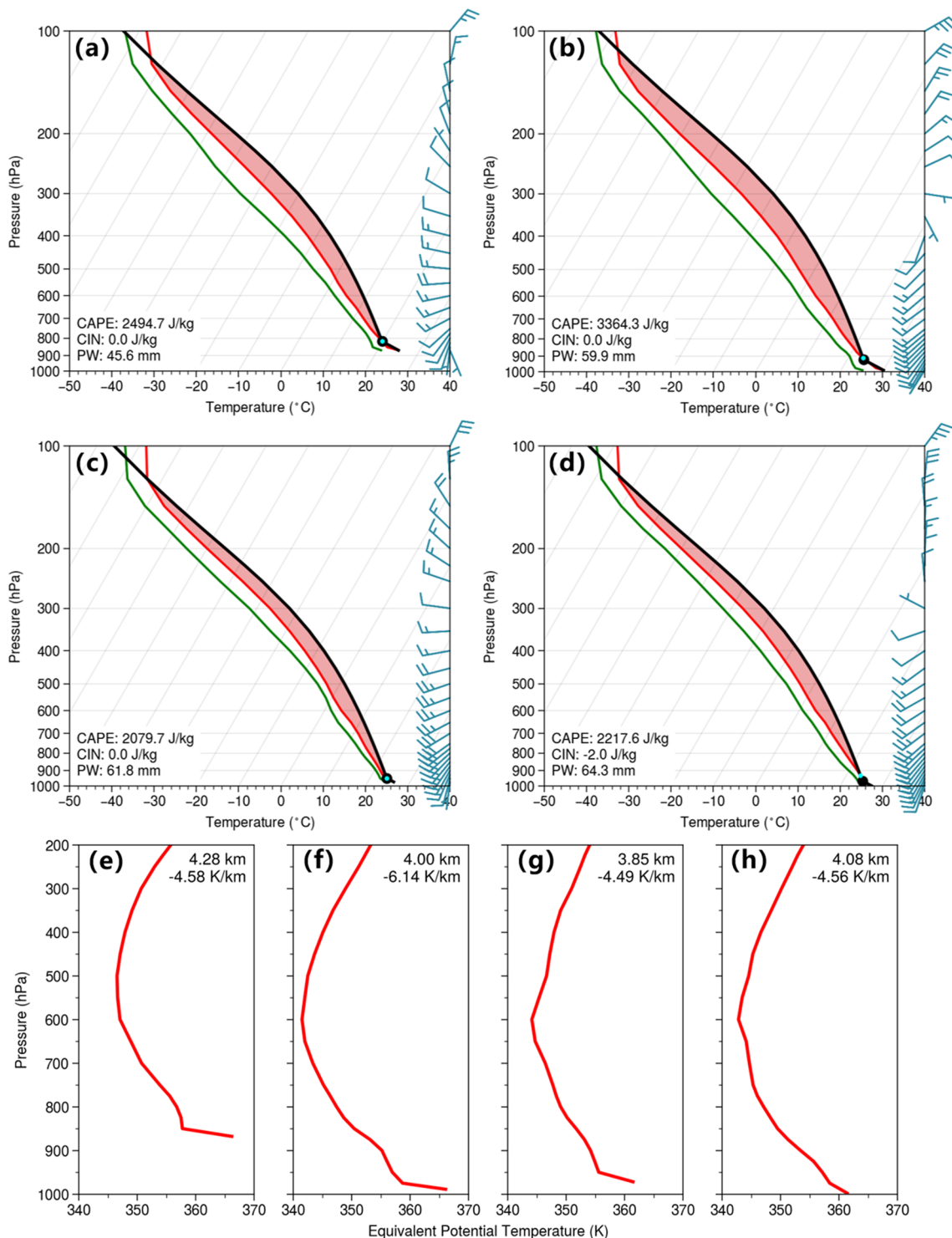


Fig. 10 The composite soundings (a–d) and the vertical profiles of equivalent potential temperature (e–h) 3 h before MCS formations over YGP (a, e), Hainan Island (b, f), MT (c, g) and CS (d, h). The large black (small blue) dots on the soundings represent the lifting condensation level (the level of free convection). The values of con-

vective available potential energy (CAPE), convective inhibition (CI) and precipitable water (PW) are labeled on the left-bottom corner on (a)–(d). The depths of the convective unstable layer (upper) and the mean lapse rates of equivalent potential temperature (lower) are labeled on the right-top corner on (e)–(h)

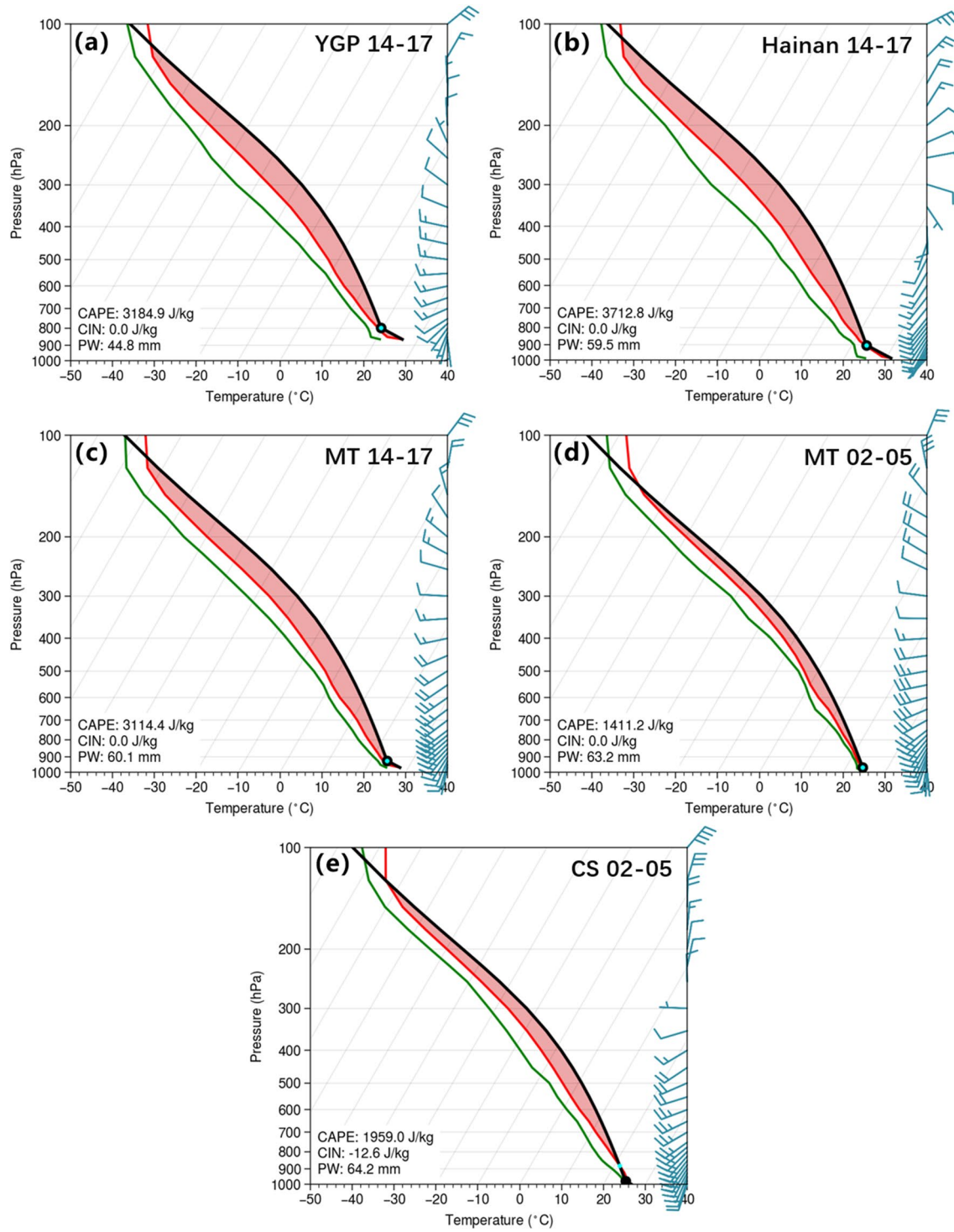


Fig. 11 The composite soundings 3 h before the formations of MCS forming at the peak time (labeled on the right top corner) over YGP (a), Hainan Island (b), MT (c, d) and CS (e). The large black (small blue) dots on the soundings represent the lifting condensation level (the level of free convection). The values of convective available

potential energy (CAPE), convective inhibition (CI) and precipitable water (PW) are labeled on the left-bottom corner on. Note that Fig. 10 shows that the diurnal variation for MCSs over MT has two peaks at 1400–1700 BST (c) and 0200–0500 BST (d), respectively

condensation level and low level of free convection, which both favor the convection. The comparison between the LLJs of MT and CS shows that the wind speed is larger and the jet core is higher of MT than those of CS. With a large wind speed and a high jet core (Fig. 10c), the LLJ of MT penetrates farther north and interacts with the mountains in northern GD and GX (Fig. 9e), providing mechanism for the convection initiation. However, with a smaller wind speed and a lower jet core (Fig. 10d), the LLJ of CS locates relatively south, interacts with the coast in southern GD (Fig. 9g) and initiates convection. Note that the double peaks of MCS formation over MT (Fig. 8c) suggesting that the LLJs interacting with mountains may not be the only mechanism for the convection initiation over this region, and that the local diabatic effect and the diurnal variation of the front may also be responsible for the MCS formation over MT (Liu et al. 2023).

To further illustrate the characteristics of environmental conditions for the MCSs forming at the peak time (Fig. 8), the composite soundings for these cases are calculated and the results are shown in Fig. 11. The environmental conditions of the afternoon peaks feature high-value CAPE and relatively weak vertical wind shear, whereas the environmental conditions of the nocturnal peaks feature low-value CAPE and strong vertical wind shear. This phenomenon is obvious when comparing the diurnal peak (with CAPE of 3114.4 J kg^{-1} and $0\text{--}3 \text{ km}$ vertical wind shear of 8.91 m s^{-1} , Fig. 10 c), and nocturnal peak (with CAPE of 1411.2 J kg^{-1} and $0\text{--}3 \text{ km}$ vertical wind shear of 11.48 m s^{-1} , Fig. 10 d) over MT. Note that the soundings corresponding to the afternoon peaks (Fig. 10 a, b, and c) exhibit super adiabatic temperature profiles at the lower levels, accompanied by very large CAPE, indicating that solar radiation plays an important role in the afternoon peak. While in the soundings corresponding to the early morning peaks, the prominent features are the strong low-level winds, suggesting that the LLJs are related to the formation of MCSs in the early morning.

Laing and Fritsch (2000) found that MCCs initiated with in prominent baroclinic zones characterized by large values of vertical wind shear and CAPE and that the low-level jets, the warm advection and the local maximum in absolute humidity played important roles in the formation of the convective systems. All of the above-mentioned features have been found in the environmental conditions favorable for MCS formation during the DBRS of 2022, although the relative importance of each feature appears to differ between the four regions.

5 Conclusions

By utilizing the hourly rainfall data, the brightness temperature data and the ERA5 reanalysis data, the general characteristics of the extreme rainfall during the DBRS of 2022

are quantitatively described first, then the configurations of the weather systems and their contributions to the extreme rainfall are analyzed from the synoptic-scale, and finally the features of the MCSs responsible for the extreme rainfall and the environmental conditions favorable for the MCS formation are studied. The main conclusions are described as follows.

- 1) The total rainfall amount during the DBRS of 2022 is the largest since 1981, with 70 out of 347 national rain gauge stations ranking at the top in history. It is found that much larger (smaller) rainfall amount locates in the northern (southern) part of South China compared with the climatology. Both the hourly rain rate and the rainfall frequency are higher than the climatology in the northern part of South China.
- 2) The abnormal circulation and thermodynamic conditions are mainly responsible for the extreme rainfall during the DBRS of 2022. The abnormal moisture transportation and convergence together with the frontal zone during the DBRS of 2022, which is stronger than the climatology, results in the rainfall centers over the northern part of South China.
- 3) The following synoptic-systems are active and favorite for formation of rainfall during the DBRS of 2022. The deep warm air advection and convective instability ahead of the frontal zone combined with orographic lifting results in the upward motion of the warm-moist air mass. At the exit of the LLJ, the convergence of the southwesterly flow and the northerly flow provides synoptic-scale ascent, favorable for the initiation of convective cells and their subsequent organization into the MCS and rainfall production. Similar configurations repeatedly impact South China during the DBRS of 2022, causing multiple heavy rainfall events, leading to the extreme rainfall.
- 4) During the DBRS of 2022, 54.35% of the rainfall amount is related to the MCS. The MCSs causing the rainfall over South China originate from 4 regions, namely the YGP, the northeastern Indo-China Peninsula, the Hainan Island, the mountains over northeastern GX and northern GD (MT) and the coastal areas over southern GD(CS). The MCSs in the four regions are characterized by different formation peaks, spatial scales, lifetimes and propagations. The MCSs from the YGP tend to form in the afternoon or early evening, and propagate eastward after formation.
- 5) The composite analysis of circulations suggests that the MCSs from 4 regions all tend to form ahead of mid-level troughs at 700 hPa, within a deep and strong convective instability. The MCSs from YGP form in the large-scale warm-moist air mass, which provides instability for the MCSs' formation. The moistening caused by synoptic

advection and the local diabatic heating enhance the convective instability over Hainan Island. The abundant moisture supply related to the LLJs produces strong convective instability, low lifting condensation level and low level of free convection, which favor the convection over the MT and CS. The environmental conditions of the afternoon and nocturnal MCS peaks are results of high-value CAPE and strong vertical wind shear, respectively.

The present study clarifies the mechanism of the extreme rainfall during the DBRS of 2022 from both the synoptic-scale and mesoscale perspectives. However, the above-mentioned conclusions can be further extended and enhanced with the usage of dense observations and high-resolution numerical simulations. More in-depth and detailed research will be conducted in the future in order to examine the finer structure of weather systems responsible for the extreme rainfall from formation and structure of meso-scale systems.

Acknowledgements This work was supported by the National Key R&D Program of China (Grant No. 2019YFC1510400), the National Natural Science Foundation of China (Grant 42075002), and the National Key Scientific and Technological Infrastructure project “Earth System Numerical Simulation Facility” (EarthLab).

Funding Key Technologies Research and Development Program, 2019YFC1510400, JianHua Sun. National Natural Science Foundation of China, 42075002, Shenming Fu.

Data availability The hourly rainfall observation data is obtained from <http://data.cma.cn/> with approval by China Meteorological Administration. The FY-4A BT data can be downloaded from <http://satellite.nsmc.org.cn/PortalSite/Data/Satellite.aspx> with approval by the China Meteorological Administration. The ERA5 hourly data on pressure levels is available at <https://doi.org/10.24381/cds.bd0915c6>. The ERA5 hourly data on single levels is available at <https://doi.org/10.24381/cds.adbb2d47>.

Declarations

Conflict of interest The authors declare that they have no conflict of interest.

References

- Ai, Y., Li, W., Meng, Z., Li, J.: Life cycle characteristics of MCSs in middle east China tracked by geostationary satellite and precipitation estimates. *Mon. Weather Rev.* **144**, 2517–2530 (2016). <https://doi.org/10.1175/MWR-D-15-0197.1>
- Bao, M.: The statistical analysis of the persistent heavy rain in the last 50 years over China and their backgrounds on the large scale circulation. *Chin. J. Atmos. Sci. (in Chinese)* **31**, 779–792 (2007). <https://doi.org/10.3878/j.issn.1006-9895.2007.05.03>
- Bretherton, C.S., Peters, M.E., Back, L.E.: Relationships between water vapor path and precipitation over the tropical oceans. *J. Clim.* **17**, 1517–1528 (2004). [https://doi.org/10.1175/1520-0442\(2004\)017%3c1517:RBWVPA%3e2.0.CO;2](https://doi.org/10.1175/1520-0442(2004)017%3c1517:RBWVPA%3e2.0.CO;2)
- Chen, H., Zhao, S.: Heavy rainfalls in South China and related circulation during HUAMEX period. *Chin. J. Atmos. Sci. (in Chinese)* **28**, 32–47 (2004). <https://doi.org/10.3878/j.issn.1006-9895.2004.01.04>
- Chen, Y., Luo, Y., Liu, B.: General features and synoptic-scale environments of mesoscale convective systems over South China during the 2013–2017 pre-summer rainy seasons. *Atmos. Res.* **266**, 105954 (2022). <https://doi.org/10.1016/j.atmosres.2021.105954>
- Cheng, J., Zhao, Y., Zhi, R., Feng, G.: Meridional circulation dominates the record-breaking “Dragon Boat Water” rainfall over south China in 2022. *Front. Earth Sci.* **10**, 1032313 (2023). <https://doi.org/10.3389/feart.2022.1032313>
- Du, Y., Chen, G.: Climatology of low-level jets and their impact on rainfall over southern China during the early-summer rainy season. *J. Clim.* **32**, 8813–8833 (2019). <https://doi.org/10.1175/JCLI-D-19-0306.1>
- Du, Y., Zhang, Q., Chen, Y., Zhao, Y., Wang, X.: Numerical simulations of spatial distributions and diurnal variations of low-level jets in China during early summer. *J. Clim.* **27**, 5747–5767 (2014). <https://doi.org/10.1175/JCLI-D-13-00571.1>
- Feng, Z., Houze, R.A., Leung, L.R., Song, F., Hardin, J.C., Wang, J., Gustafson, W.I., Homeyer, C.R.: Spatiotemporal characteristics and large-scale environments of mesoscale convective systems east of the Rocky Mountains. *J. Clim.* **32**, 7303–7328 (2019). <https://doi.org/10.1175/JCLI-D-19-0137.1>
- Fu, S., Zhang, J., Luo, Y., Yang, W., Sun, J.: Energy paths that sustain the warm-sector torrential rainfall over South China and their contrasts to the frontal rainfall: A case study. *Adv. Atmos. Sci.* **39**, 1519–1535 (2022). <https://doi.org/10.1007/s00376-021-1336-z>
- Guo, Y., Du, Y., Lu, R., Feng, X., Li, J., Zhang, Y., Mai, Z.: The characteristics of mesoscale convective systems generated over the Yunnan-Guizhou Plateau during the warm seasons. *Int. J. Climatol.* **42**, 7321–7341 (2022). <https://doi.org/10.1002/joc.7647>
- Hersbach, H., Bell, B., Berrisford, P., Hirahara, S., Horányi, A., Muñoz-Sabater, J., Nicolas, J., Peubey, C., Radu, R., Schepers, D., Simmons, A., Soci, C., Abdalla, S., Abellán, X., Balsamo, G., Bechtold, P., Biavati, G., Bidlot, J., Bonavita, M., De Chiara, G., Dahlgren, P., Dee, D., Diamantakis, M., Dragani, R., Fleming, J., Forbes, R., Fuentes, M., Geer, A., Haimberger, L., Healy, S., Hogan, R.J., Hólm, E., Janisková, M., Keeley, S., Laloyaux, P., Lopez, P., Lupu, C., Radnoti, G., de Rosnay, P., Rozum, I., Vamborg, F., Villaume, S., Thépaut, J.-N.: The ERA5 global reanalysis. *Q. J. r. Meteorol. Soc.* **146**, 1999–2049 (2020). <https://doi.org/10.1002/qj.3803>
- Houze, R. A. Mesoscale convective systems. *Rev. Geophys.*, 42, RG4003 (2004). <https://doi.org/10.1029/2004RG000150>
- Hu, Y., Du, Y., Luo, X.: Precipitation patterns during the “dragon boat water” in South China for the recent 49 years. *Meteorol. Mon. (in Chinese)* **39**, 1031–1041 (2013). <https://doi.org/10.7519/j.issn.1000-0526.2013.08.010>
- Kuo, Y.-H., Neelin, J.D., Mechoso, C.R.: Tropical convective transition statistics and causality in the water vapor–precipitation relation. *J. Atmos. Sci.* **74**, 915–931 (2017). <https://doi.org/10.1175/JAS-D-16-0182.1>
- Laing, A.G., Fritsch, J.M.: The large-scale environments of the global populations of mesoscale convective complexes. *Mon. Wea. Rev.* **128**, 2756–2776 (2000). [https://doi.org/10.1175/1520-0493\(2000\)128%3c2756:TLSEOT%3e2.0.CO;2](https://doi.org/10.1175/1520-0493(2000)128%3c2756:TLSEOT%3e2.0.CO;2)
- Li, X., Du, Y.: Statistical relationships between two types of heavy rainfall and low-level jets in South China. *J. Clim.* **34**, 8549–8566 (2021). <https://doi.org/10.1175/JCLI-D-21-0121.1>
- Lin, L., Wu, N., Huang, Z., Cai, A.: Causality analysis of infrequent dragon-boat precipitation in Guangdong province in 2008. *Meteorol. Mon. (in Chinese)* **35**, 43–50 (2009). <https://doi.org/10.7519/j.issn.1000-0526.2020.11.003>

- Liu, R., Sun, J., Chen, B.: Selection and classification of warm-sector heavy rainfall events over South China. *Chin. J. Atmos. Sci.* (in Chinese) **43**, 119–130 (2019). <https://doi.org/10.3878/j.issn.1006-9895.1803.17245>
- Liu, X., Luo, Y., Huang, L., Zhang, D.-L., Guan, Z.: Roles of double low-level jets in the generation of coexisting inland and coastal heavy rainfall over South China during the presummer rainy season. *J. Geophys. Res. Atmos.* **125**, e2020JD032890 (2020). <https://doi.org/10.1029/2020JD032890>
- Liu, H., Meng, Z., Zhu, Y., Huang, Y.: Convection initiation associated with a boundary layer convergence line over a real-world sharp vegetation-contrast area. *Mon. Wea. Rev.* **151**, 1189–1212 (2023). <https://doi.org/10.1175/MWR-D-22-0083.1>
- Luo, Y., Wang, H., Zhang, R., Qian, W., Luo, Z.: Comparison of rainfall characteristics and convective properties of monsoon precipitation systems over South China and the Yangtze and Huai River basin. *J. Clim.* **26**, 110–132 (2013). <https://doi.org/10.1175/JCLI-D-12-00100.1>
- Mai, Z., Fu, S., Sun, J.: Statistical features of two types of mesoscale convective systems (MCSs) generated over the eastern Tibetan Plateau during 16 consecutive warm seasons. *Clim. Environ. Res.* (in Chinese) **25**, 385–398 (2020). <https://doi.org/10.3878/j.issn.1006-9585.2019.19040>
- Mai, Z., Fu, S., Sun, J., Hu, L., Wang, X.: Key statistical characteristics of the mesoscale convective systems generated over the Tibetan Plateau and their relationship to precipitation and southwest vortices. *Int. J. Climatol.* **41**, E875–E896 (2021). <https://doi.org/10.1002/joc.6735>
- Maurer, V., Bischoff-Gauß, I., Kalthoff, N., Gantner, L., Roca, R., Panitz, H.-J.: Initiation of deep convection in the Sahel in a convection-permitting climate simulation for northern Africa: Deep convection in the Sahel. *Q. J. r. Meteorol. Soc.* **143**, 806–816 (2017). <https://doi.org/10.1002/qj.2966>
- Meng, Q., Yu, C.: Analysis of the June 2022 atmospheric circulation and weather. *Meteorol. Mon.* (in Chinese) **48**, 1209–1216 (2022). <https://doi.org/10.7519/j.issn.1000-0526.2022.080201>
- Meng, Y., Sun, J., Zhang, Y., Fu, S.: A 10-year climatology of mesoscale convective systems and their synoptic circulations in the southwest mountain area of China. *J. Hydrometeorol.* **22**, 23–41 (2020). <https://doi.org/10.1175/JHM-D-20-0167.1>
- Mu, J., Wang, J., Li, Z.: A study of environment and mesoscale convective systems of continuous heavy rainfall in the South of China in June 2005. *Acta Meteorol. Sin.* (in Chinese) **66**, 437–451 (2008). <https://doi.org/10.11676/qxb2008.040>
- Ninomiya, K., Ikawa, M., Akiyama, T.: Long-lived medium-scale cumulonimbus cluster in Asian subtropical humid region. *J. Meteorol. Soc. Japan Ser. II*(59), 564–577 (1981). https://doi.org/10.2151/jmsj1965.59.4_564
- Peters, J.M., Schumacher, R.S.: Objective categorization of heavy-rain-producing MCS synoptic types by rotated principal component analysis. *Mon. Weather Rev.* **142**, 1716–1737 (2014). <https://doi.org/10.1175/MWR-D-13-00295.1>
- Punkka, A.-J., Bister, M.: Mesoscale convective systems and their synoptic-scale environment in Finland. *Weather Forecast.* **30**, 182–196 (2015). <https://doi.org/10.1175/WAF-D-13-00146.1>
- Qian, W., Ai, Y., Leung, J.C.-H., Zhang, B.: Anomaly-based synoptic analysis and model product application for 2020 summer southern China rainfall events. *Atmos. Res.* **258**, 105631 (2021). <https://doi.org/10.1016/j.atmosres.2021.105631>
- Qian, W., Ai, Y., Chen, L., Li H.: Anomalous synoptic pattern of typical dragon boat precipitation process in Guangdong province. *J. Trop. Meteorol.* (in Chinese), 36, 433–443 (2020). <https://doi.org/10.16032/j.issn.1004-4965.2020.040>
- Reif, D.W., Bluestein, H.B.: A 20-year climatology of nocturnal convection initiation over the central and southern Great Plains during the warm season. *Mon. Weather Rev.* **145**, 1615–1639 (2017). <https://doi.org/10.1175/MWR-D-16-0340.1>
- Salio, P., Nicolini, M., Zipser, E.J.: Mesoscale convective systems over southeastern South America and their relationship with the South American low-level jet. *Mon. Weather Rev.* **135**, 1290–1309 (2007). <https://doi.org/10.1175/MWR3305.1>
- Schumacher, R.S., Johnson, R.H.: Organization and environmental properties of extreme-rain-producing mesoscale convective systems. *Mon. Weather Rev.* **133**, 961–976 (2005). <https://doi.org/10.1175/MWR2899.1>
- Sheng, B., Wang, H., Li, H., Wu, K., Li, Q.: Thermodynamic and dynamic effects of anomalous dragon boat water over South China in 2022. *Weather Clim. Extremes* **40**, 100560 (2023). <https://doi.org/10.1016/j.wace.2023.100560>
- Song, F., Feng, Z., Leung, L.R., Houze, R.A., Jr., Wang, J., Hardin, J., Homeyer, C.R.: Contrasting spring and summer large-scale environments associated with mesoscale convective systems over the US Great Plains. *J. Clim.* **32**, 6749–6767 (2019). <https://doi.org/10.1175/JCLI-D-18-0839.1>
- Sun, J., Zhao, S.: A diagnosis and simulation study of a strong heavy rainfall in South China. *Chin. J. Atmos. Sci.* (in Chinese) **24**, 381–392 (2000). <https://doi.org/10.3878/j.issn.1006-9895.2000.03.10>
- Sun, J., Zhang, Y., Liu, R., Fu, S., Tian, F.: A review of research on warm-sector heavy rainfall in China. *Adv. Atmos. Sci.* **36**, 1299–1307 (2019). <https://doi.org/10.1007/s00376-019-9021-1>
- Sun, J., Zhao, S.: A study of mesoscale convective systems and its environmental fields during the June 1994 record heavy rainfall of South China. Part I: A numerical simulation study of meso- β convective system inducing heavy rainfall. *Chin. J. Atmos. Sci.* (in Chinese), 26, 541–557 (2002). <https://doi.org/10.3878/j.issn.1006-9895.2002.04.11>
- Trier, S.B., Parsons, D.B.: Evolution of environmental conditions preceding the development of a nocturnal mesoscale convective complex. *Mon. Weather Rev.* **121**, 1078–1098 (1993). [https://doi.org/10.1175/1520-0493\(1993\)121%3c1078:EOECPT%3e2.0.CO;2](https://doi.org/10.1175/1520-0493(1993)121%3c1078:EOECPT%3e2.0.CO;2)
- Wang, D., Xia, R., Liu, Y.: A preliminary study of the flood causing rainstorm during the first rainy season in South China in 2008. *Acta Meteorol. Sin.* (in Chinese), 69, 137–148 (2011). <https://doi.org/10.11676/qxb2011.012>
- Wu, H., Du, Y., Qin, P.: Climate characteristics and variation of rainstorm in South China. *Meteorol. Mon.* (in Chinese) **37**, 1262–1269 (2011). <https://doi.org/10.7519/j.issn.1000-0526.2011.10.009>
- Wu, M., Luo, Y., Chen, F., Wong, W.K.: Observed link of extreme hourly precipitation changes to urbanization over coastal South China. *J. Appl. Meteorol. Climatol.* **58**, 1799–1819 (2019). <https://doi.org/10.1175/JAMC-D-18-0284.1>
- Wu, N., Wen, Z., Deng, J., Lin, L., Chen, G.: Advances in warm-sector heavy rainfall during the first rainy season in South China. *J. Meteorol. Sci.* (in Chinese) **40**, 605–616 (2020). <https://doi.org/10.3969/2020jms.0077>
- Wu, H., Li, C., Wang, D.: Analysis on characteristics and abnormal causes of dragon-boat precipitation in Guangdong in the past 55 years. *J. Trop. Meteorol.* (in Chinese), 33, 608–616 (2017). <https://doi.org/10.16032/j.issn.1004-4965.2017.05.004>
- Xia, R., Zhao, S., Sun, J.: A study of circumstances of meso- β -scale systems of strong heavy rainfall in warm sector ahead of fronts in South China. *Chin. J. Atmos. Sci.* (in Chinese) **30**, 988–1008 (2006). <https://doi.org/10.3878/j.issn.1006-9895.2006.05.26>
- Yang, X., Fei, J., Huang, X., Cheng, X., Carvalho, L.M.V., He, H.: Characteristics of mesoscale convective systems over China and its vicinity using geostationary satellite FY2. *J. Clim.* **28**, 4890–4907 (2015). <https://doi.org/10.1175/JCLI-D-14-00491.1>
- Yang, J., Zhang, Z., Wei, C., Lu, F., Guo, Q.: Introducing the new generation of Chinese geostationary weather satellites, Fengyun-4. *Bull. Am. Meteorol. Soc.* **98**, 1637–1658 (2017). <https://doi.org/10.1175/BAMS-D-16-0065.1>

- Yang, R., Zhang, Y., Sun, J., Li, J.: The comparison of statistical features and synoptic circulations between the eastward-propagating and quasi-stationary MCSs during the warm season around the second-step terrain along the middle reaches of the Yangtze River. *Sci. China Earth Sci.* **63**, 1209–1222 (2020). <https://doi.org/10.1007/s11430-018-9385-3>
- Zhang, Y., Sun, J., Yang, R., Ma, R.: Initiation and evolution of long-lived eastward-propagating mesoscale convective systems over the second-step terrain along Yangtze-Huaihe River valley. *Adv. Atmos. Sci.* **39**, 763–781 (2022). <https://doi.org/10.1007/s00376-022-1303-3>
- Zhao, Y., Li, Z., Xiao Z.: Comparison analysis of South China front and warm-area heavy rain systems in June 2006. *Meteorol. Sci. Technol. (in Chinese)*, **36**, 47–54 (2008). <https://doi.org/10.19517/j.1671-6345.2008.01.011>
- Zheng, L., Sun, J., Zhang, X., Liu, C.: Organizational modes of mesoscale convective systems over central East China. *Weather Forecast.* **28**, 1081–1098 (2013). <https://doi.org/10.1175/WAF-D-12-00088.1>
- Zhu, L., Bai, L., Chen, G., Sun, Y. Q., Meng, Z.: Convection initiation associated with ambient winds and local circulations over a tropical island in South China. *Geophys. Res. Lett.*, **48**, e2021GL094382 (2021). <https://doi.org/10.1029/2021GL094382>

Publisher's Note Springer Nature remains neutral with regard to jurisdictional claims in published maps and institutional affiliations.

Springer Nature or its licensor (e.g. a society or other partner) holds exclusive rights to this article under a publishing agreement with the author(s) or other rightsholder(s); author self-archiving of the accepted manuscript version of this article is solely governed by the terms of such publishing agreement and applicable law.